J. Fluid Mech. (2017), *vol.* 817, R3, doi:10.1017/jfm.2017.97



JFM RAPIDS
journals.cambridge.org/rapids

Sustaining processes from recurrent flows in body-forced turbulence

Dan Lucas[1,†] **and Rich Kerswell**[2]

[1]Department of Applied Mathematics and Theoretical Physics, University of Cambridge, Cambridge CB3 0WA, UK

[2]School of Mathematics, University of Bristol, University Walk, Bristol BS8 1TW, UK

(Received 15 November 2016; revised 9 February 2017; accepted 12 February 2017; first published online 24 March 2017)

By extracting unstable invariant solutions directly from body-forced three-dimensional turbulence, we study the dynamical processes at play when the forcing is large scale and unidirectional in either the momentum or the vorticity equations. In the former case, the dynamical processes familiar from recent work on linearly stable shear flows – variously called the self-sustaining process (Waleffe, *Phys. Fluids*, vol. 9 (4), 1997, pp. 883–900) or vortex–wave interaction (Hall & Smith, *J. Fluid Mech.*, vol. 227, 1991, pp. 641–666; Hall & Sherwin, *J. Fluid Mech.*, vol. 661, 2010, pp. 178–205) – are important even when the base flow is linearly unstable. In the latter case, where the forcing drives Taylor–Green vortices, a number of mechanisms are observed from the various types of periodic orbits isolated. In particular, two different transient growth mechanisms are discussed to explain the more complex states found.

Key words: chaos, nonlinear dynamical systems, turbulent flows

1. Introduction

The chaotic and multiscale nature of turbulent flows continues to challenge the understanding of fluid dynamicists. One route to penetrating such a mathematically demanding system is to view a turbulent flow as a trajectory through a high-dimensional phase space (Hopf 1948). This trajectory then passes near the vicinity of unstable solutions and accumulates characteristics of these states which can be extracted, via numerical computation, for thorough investigation. Such an approach has been pioneered for wall-bounded shear flows (Kawahara & Kida 2001; Viswanath 2007; Cvitanović & Gibson 2010; Kawahara, Uhlmann & van Veen 2012; Kreilos & Eckhardt 2012; Willis, Short & Cvitanovic 2016), two-dimensional (2D) body-forced Kolmogorov flow (Chandler & Kerswell 2013; Lucas & Kerswell 2015) and highly symmetric isotropic turbulence (van Veen, Kida & Kawahara 2006).

These unstable states, in particular the time-dependent recurrent flows or UPOs (unstable periodic orbits), contain valuable dynamical information which may provide

†Email address for correspondence: dl549@cam.ac.uk

© Cambridge University Press 2017

https://doi.org/10.1017/jfm.2017.97 Published online by Cambridge University Press

some predictability to the inherent complexity of the turbulence. This has been addressed through the application of 'periodic orbit theory' (Cvitanović 1992), whereby the statistics of individual UPOs are combined weighted by their relative stability in an attempt to rationalise the turbulent statistics. Recent work (Lan & Cvitanović 2004; Chandler & Kerswell 2013; Lucas & Kerswell 2015) has assessed the effectiveness of this strategy and discussed computational nuances. Rather than attempt this for three-dimensional Kolmogorov flow, we use the extracted recurrent flows as a guide for what complicated and interlinked physical processes may underpin the turbulence. A very successful example of such an approach is plane Couette flow, where a nearly recurrent flow was found (Hamilton, Kim & Waleffe 1995), which suggested the 'self-sustaining process' (Waleffe 1997), subsequently found manifested in a UPO extracted from turbulent data (Kawahara & Kida 2001). We consider three-dimensional flow, since this permits a greater variety of forcing than our previous 2D study (Lucas & Kerswell (2015); see also van Veen & Goto (2016) for a recent three-dimensional (3D) study with the usual monochromatic forcing), in particular enabling a comparison between shear-driven (e.g. plane Couette flow) and vortically driven turbulence. The vortical case has been examined previously for sustaining processes (Goto 2008, 2012; Yasuda, Goto & Kawahara 2014; Goto, Saito & Kawahara 2017) and so is a natural choice to tackle with a recurrent flow analysis.

2. Formulation

We consider the three-dimensional body-forced incompressible Navier–Stokes equations,

$$\frac{\partial \boldsymbol{u}}{\partial t} + \boldsymbol{u}\cdot\nabla\boldsymbol{u} + \nabla p = \frac{1}{Re}\Delta\boldsymbol{u} + \boldsymbol{f}, \tag{2.1}$$

$$\nabla\cdot\boldsymbol{u} = 0, \tag{2.2}$$

where the Reynolds number is defined as $Re := \sqrt{\chi}/\nu(L_f/2\pi)^{3/2}$, with L_f the forcing length scale, χ the forcing amplitude and ν the kinematic viscosity, having non-dimensionalised the equations with length scale $L_f/2\pi$ and time scale $\sqrt{L_f/2\pi\chi}$ (see, e.g., Chandler & Kerswell 2013; Lucas & Kerswell 2014). Two forms of forcing are considered – the first, $\boldsymbol{f}_u = \sin 2y \sin 2z\hat{\boldsymbol{x}}$, driving a unidirectional basic flow $\boldsymbol{u}_{lam} := (1/8)Re \sin 2y \sin 2z\hat{\boldsymbol{x}}$ and the second, $\boldsymbol{f}_\omega := \sin 2y \cos 2z\hat{\boldsymbol{y}} - \cos 2y \sin 2z\hat{\boldsymbol{z}}$, driving a unidirectional vorticity $\boldsymbol{\omega}_{lam} := (1/2)Re \sin 2y \sin 2z\hat{\boldsymbol{x}}$, where vorticity is defined as $\boldsymbol{\omega} = \xi\hat{\boldsymbol{x}} + \eta\hat{\boldsymbol{y}} + \zeta\hat{\boldsymbol{z}} = \nabla\times\boldsymbol{u}$. The equations were solved over the periodic cube $[0, 2\pi]^3$ using a fully dealiased (two-thirds rule) pseudospectral method implemented in CUDA to run on a GPU card (see Lucas & Kerswell 2014 for details). A resolution of 128^3 was used throughout, which allowed the code to run locally (and efficiently) on a single GPU card (an M2090 6 GB Tesla card), and the flow field was initiated in Fourier space on the shell $2.5 \leqslant |\boldsymbol{k}| \leqslant 9.5$ with complex coefficients having uniform amplitudes but randomly distributed phases such that the total enstrophy $\langle|\boldsymbol{\omega}|^2\rangle_V := 1/(2\pi)^3 \iiint |\boldsymbol{\omega}|^2 \,\mathrm{d}x\,\mathrm{d}y\,\mathrm{d}z = 1$. To uncover recurrent processes embedded in the turbulent attractor, a very long direct numerical simulation (DNS) data set was produced, and episodes where the flow appeared to almost repeat were identified on the fly. Flow fields from these episodes were then used to search for exactly recurring flow solutions using a Newton–GMRES–hookstep algorithm (Viswanath 2007; Chandler & Kerswell 2013; Lucas & Kerswell 2015) which took months of CPU time even with GPU acceleration. Every recurring solution found was examined for its underlying dynamical processes.

https://doi.org/10.1017/jfm.2017.97 Published online by Cambridge University Press

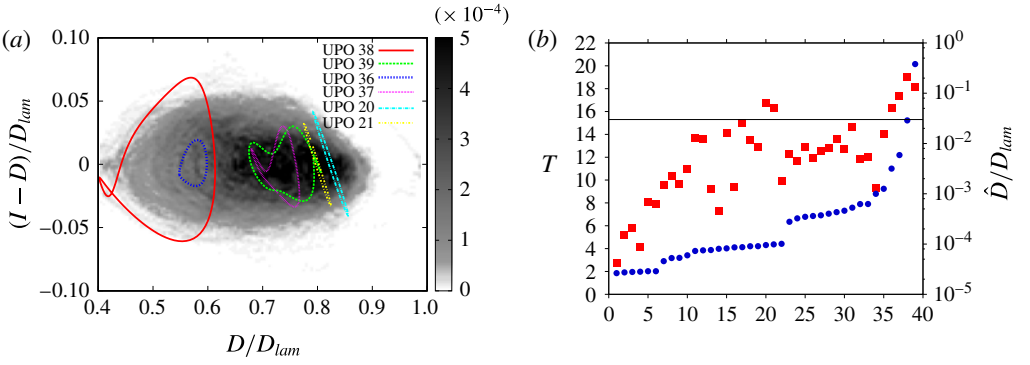


FIGURE 1. (*a*) Projection of dynamics onto the normalised D–$(I-D)$ plane, where $I = \langle \boldsymbol{u}\cdot\boldsymbol{f}_u\rangle_V$ is the energy input rate and $D = \langle|\boldsymbol{\nabla u}|^2\rangle_V/Re$ is the dissipation rate. Grey colours represent the probability density function (p.d.f.) of the DNS with forcing $\boldsymbol{f}_u$ and lines represent converged unstable periodic orbits. (*b*) Distribution of period T (blue circles) and normalised dissipation range $\hat{D}/D_{lam}$ (red squares) over the UPOs found.

3. Results

3.1. *Case* $\boldsymbol{f}_u$

At $Re = 20$ (and $R_{thres} = 0.8$ – see Lucas & Kerswell 2015), a DNS data set of duration $T = 6\times10^4$ (in units of $\sqrt{L_f/2\pi\chi}$) yielded a total of 233 recurrent episodes which allowed 64 recurrent flows – 39 UPOs, 19 travelling waves (TWs) and six equilibria (EQs) – to be converged. The UPOs found are documented in figure 1 (and the supplemental material available at https://doi.org/10.1017/jfm.2017.97). Unstable periodic orbits of longer period are more difficult to isolate because they tend to be more strongly unstable (both larger unstable growth rates and more unstable directions) than shorter-period UPOs, and as a result near-recurrent episodes in the DNS are rarer and subsequent convergence is more challenging. However, longer-period orbits tend to span the turbulent attractor better (as measured by $\hat{D}/D_{lam} := (\max D(t) - \min D(t))/D_{lam}$, where $D = \langle|\boldsymbol{\nabla u}|^2\rangle_V/Re$ is the total dissipation) and should be more representative of the dynamical processes at play, so we concentrate on these subsequently. A threshold of $\hat{D} = 0.03D_{lam}$ (see figure 1*b*) picks out six UPOs – 20, 21, 36, 37, 38, 39 – which are compared with a probability density function (p.d.f.) of the DNS in figure 1(*a*).

Of these UPOs, the final four show the characteristic features of the self-sustaining-process (SSP)/vortex–wave-interaction (VWI) theory of wall-bounded shear flows in that the peak amplitudes of (small) streamwise rolls, streaks and (streamwise-dependent) waves are respectively staggered in time. The now well-known loop of events (Hall & Smith 1991; Waleffe 1997; Hall & Sherwin 2010) that produce this starts with the streamwise rolls advecting the underlying shear to drive streaks, which, when they are large enough, become unstable to streamwise-dependent waves. These waves then grow by extracting energy from the streaks (which then diminish) and through wave–wave self-interaction re-energise the rolls, whereupon the process repeats. What is interesting is that the SSP/VWI process is usually invoked to explain the existence of solutions other than the basic state when the latter is linearly stable. Here, we find the same process to be operative even though the basic state is linearly unstable. To show this, the flow field of UPO 39 with the laminar state subtracted

https://doi.org/10.1017/jfm.2017.97 Published online by Cambridge University Press

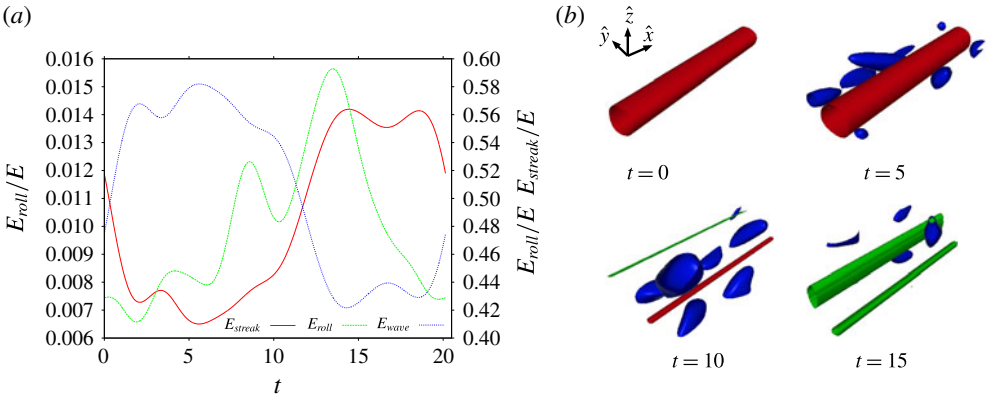


FIGURE 2. Plots showing the SSP decomposition for UPO 39. (*a*) Time series for the energies E_{streak} (red), E_{roll} (green) and E_{wave} (blue). (*b*) Isosurfaces for the velocity components contributing to these energies ($\bar{u}_p = 0.75$, red; $\sqrt{\bar{v}_p^2 + \bar{w}_p^2} = 0.13$, green; $|\boldsymbol{u}_p - \bar{\boldsymbol{u}}_p| = 1$, blue) for a subdomain chosen to best illustrate the loop of dynamics involving streaks, waves and rolls.

($\boldsymbol{u}_p := \boldsymbol{u} - \boldsymbol{u}_{lam} = u_p\hat{\boldsymbol{x}} + v_p\hat{\boldsymbol{y}} + w_p\hat{\boldsymbol{z}}$) is decomposed into streaks $\overline{u}_p\hat{\boldsymbol{x}}$, rolls $\overline{v}_p\hat{\boldsymbol{y}} + \overline{w}_p\hat{\boldsymbol{z}}$ and streamwise-dependent waves $\boldsymbol{u}_p - \overline{\boldsymbol{u}}_p$, with the corresponding energies being defined as

$$E_{streak} = \tfrac{1}{2}\langle \overline{u}_p^2 \rangle, \quad E_{roll} = \tfrac{1}{2}\langle \overline{v}_p^2 + \overline{w}_p^2 \rangle, \quad E_{wave} = \tfrac{1}{2}\langle (\boldsymbol{u}_p - \overline{\boldsymbol{u}}_p)^2 \rangle, \qquad (3.1a\text{–}c)$$

so that $E := \langle \boldsymbol{u}_p^2 \rangle/2 = E_{streak} + E_{roll} + E_{wave}$, where $\overline{(\cdot)} := \int_0^{2\pi} (\cdot)\,\mathrm{d}x/2\pi$ and $\langle (\cdot) \rangle := \int\int\int (\cdot)\,\mathrm{d}x\,\mathrm{d}y\,\mathrm{d}z/(2\pi)^3$. Figure 2 shows time series for these energies, relative to the total energy, and 3D isosurfaces for a subregion best exhibiting the regeneration cycle (secondary frequencies in the time series relate to individual streaks undergoing an SSP cycle in/out of phase with each other): initially large streaks ($t = 0$) pump their energy into the wave field ($t = 5$), which then decays, pouring energy into the rolls ($t = 10$ and $t = 15$), which subsequently drive the streaks. A similar plot for UPO 38 is included in the supplementary material to demonstrate the generality of this picture.

The key component of the SSP/VWI mechanism (in the simplest steady setting) is the presence of a neutral (small-amplitude) wave mode riding on the much larger streamwise-averaged streamwise flow $\overline{u}(y, z)\hat{\boldsymbol{x}}$. For a linearly stable base flow $u_{lam}(y, z)\hat{\boldsymbol{x}}$, small finite-amplitude rolls are required to adjust this to make it marginally stable (with the neutral mode so generated nonlinearly feeding back to sustain the rolls). For a linearly unstable flow, the same can clearly still happen, but now the rolls can act to stabilise $u_{lam}(y, z)\hat{\boldsymbol{x}}$ by making one (or perhaps more) unstable wave mode(s) on $u_{lam}(y, z)\hat{\boldsymbol{x}}$ neutral on $\overline{u}(y, z)\hat{\boldsymbol{x}}$. The same thinking carries over to the more generic time-periodic situation, with the rolls generating streamwise flows that are on average neutrally stable to a wave mode (or collection of wave modes). For example, there are 12/18 unstable directions of the streak field $\overline{u}_p$ for UPOs 38/39 when the streak field is maximum and 2/14 when it is minimum. This would then create finite-amplitude states through saddle node bifurcations familiar from flows like plane Couette flow and pipe flow typically unconnected to the laminar state (e.g. see UPO 38 in figure 3*b*).

https://doi.org/10.1017/jfm.2017.97 Published online by Cambridge University Press

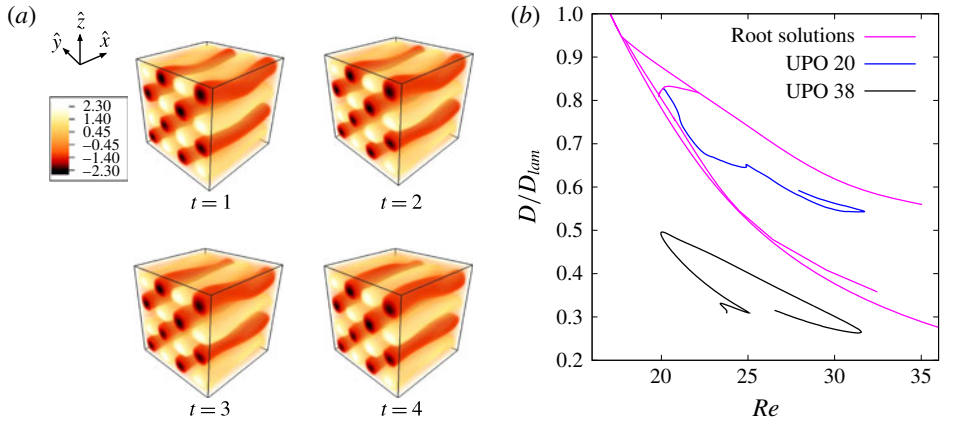


FIGURE 3. (*a*) A rendering of the streamwise velocity, $u\hat{\boldsymbol{x}}$, for UPO 20 at four snapshots. This shows the propagation of long-wavelength streamwise disturbances along the base flow. (*b*) A bifurcation diagram for UPOs 20 and 38 showing, through a sequence of bifurcations (three), the connection to the base flow u_{lam} (where $D/D_{lam} = 1$) at $Re \approx 17$ for UPO 20, but no such connections for UPO 38.

Since u_{lam} is unstable, there are also 'derivative' states which arise through a continuous sequence of bifurcations off the laminar state; UPO 20 is a typical example shown in figure 3(*a*). Long-wavelength streamwise disturbances propagate on top of the base flow, consistent with the long-wavelength instability of Kolmogorov flow (Meshalkin & Sinai 1961), and the streak field is small and varies very little. As a result, there is no stability change of $u(y, z)\hat{\boldsymbol{x}}$ for UPO 20 over a cycle: 20 unstable directions are always found for $\overline{u}_p$ compared with the 32 unstable directions for $u_{lam}(y, z)\hat{\boldsymbol{x}}$. Since both SSP/VWI UPOs and 'derivative' UPOs have been extracted directly from turbulent DNS at $Re = 20$ (and by implication are therefore embedded in the turbulent attractor), the overall conclusion of our computations at $Re = 20$ is that both are dynamically important in the complex dynamics observed.

At $Re = 30$, a time integration of $T = 1.6 \times 10^5$ finds 67 guesses; however, none of these can be converged to invariant solutions presumably because these are becoming more unstable. To quantify this, all six large-$\hat{D}$ UPOs were continued up in Re from 20 using the arclength continuation. All continuations quickly turned back (figure 3 shows two such continuations), retreating to lower Re, with only three out of the six UPOs (UPOs 20, 21 and 38) extending beyond $Re = 30$. UPO 21 reaches the furthest ($Re = 42$), and by then its instability has considerably increased by two complementary measures: (*a*) the sum of the unstable growth rates more than quadruples and (*b*) the number of unstable directions jumps from 20 to 93. The other UPOs show similar rapid destabilisation (e.g. the dimension of the unstable manifold for UPO 37 jumps from 15 at $Re = 20$ to 58 at $Re = 27$, while that for UPO 20 increases from 25 at $Re = 20$ to 67 at $Re = 30$). These figures suggest that the dimension of the chaotic attractor very quickly increases as Re increases beyond 20.

3.2. *Case* $\boldsymbol{f}_\omega$

For unidirectional vorticity forcing at $Re = 15$, a DNS of duration $T = 10^4$ with $R_{thres} = 0.8$ yielded a total of 600 recurrent episodes, from which 22 unstable

https://doi.org/10.1017/jfm.2017.97 Published online by Cambridge University Press

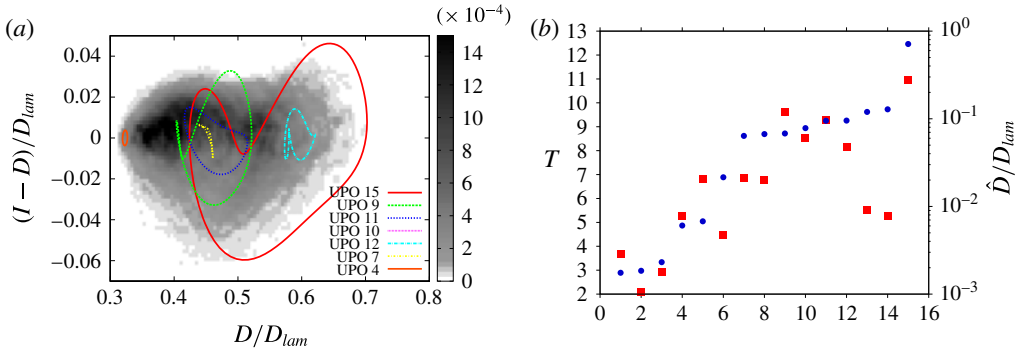


FIGURE 4. (*a*) Projection of dynamics onto the normalised D–$(I-D)$ plane, where $I = \langle \boldsymbol{u} \cdot \boldsymbol{f}_u \rangle_V$ is the energy input rate and $D = \langle |\nabla \boldsymbol{u}|^2 \rangle_V / Re$ is the dissipation rate. Grey colours represent the p.d.f. of the DNS with forcing $\boldsymbol{f}_\omega$ and lines represent converged unstable periodic orbits. (*b*) Distribution of period T (blue circles) and normalised dissipation range $\hat{D}/D_{lam}$ (red squares) over the set of 15 UPOs.

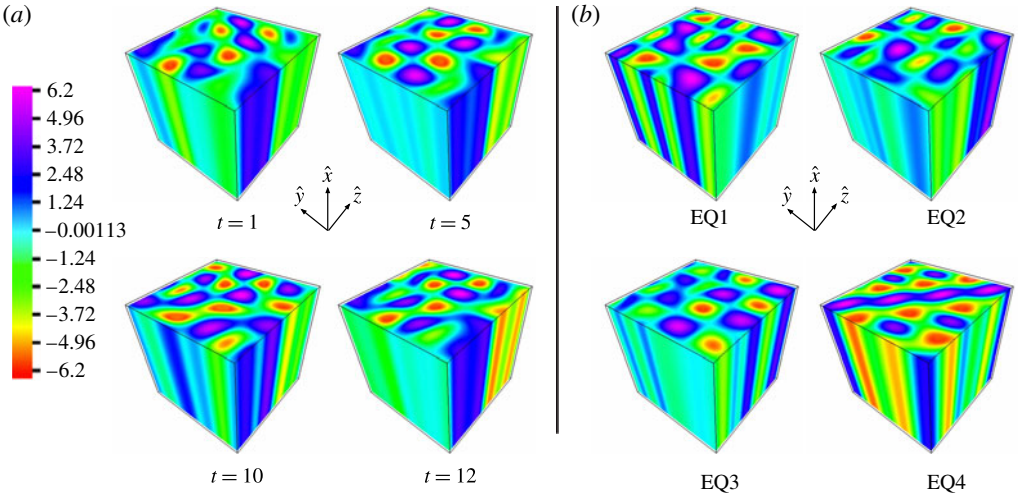


FIGURE 5. Snapshots in isometric view of the axial vorticity ξ for the two-dimensional UPO 15 (*a*) and steady states EQ1–4 (*b*) in the case $\boldsymbol{f}_\omega$.

recurrent flows – 15 UPOs, three TWs and four EQs – were converged with the Newton–GMRES–hookstep algorithm. Figure 4 shows the projection of the six UPOs with largest $\hat{D}$ and a p.d.f. of the DNS trajectory on the $(I-D)/D_{lam}$ versus D/D_{lam} plane. These solutions can be classified into three categories.

The simplest solutions are two-dimensional. As an example, UPO 15, which has the largest $\hat{D}$, shows a classical 2D loop of vortex merger and splitting with no variations in the x direction. This type of process was examined in detail in 2D Kolmogorov flow in Lucas & Kerswell (2015). All four equilibria are 2D states and are shown in figure 5.

The second type of solution breaks the x-translational symmetry, but shows quite low-amplitude time dependence in the form of vortex waves (Kelvin modes) on the basic vortex tubes. This describes most of the low-amplitude (small-$\hat{D}$) UPOs, with figure 6 showing an example, UPO 4, which was the UPO converged most frequently

https://doi.org/10.1017/jfm.2017.97 Published online by Cambridge University Press

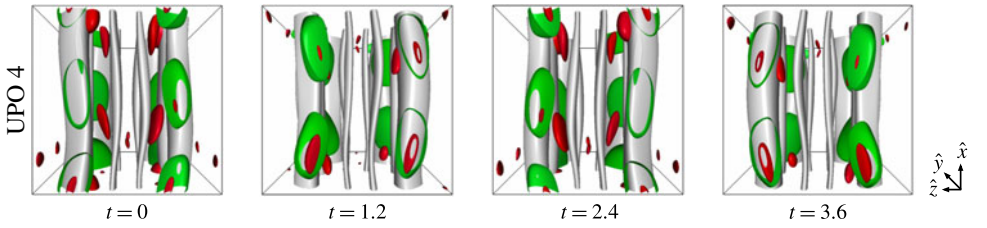


FIGURE 6. Isometric view of vorticity isosurfaces ($|\xi| = 3$ coloured grey, $|\eta| = 0.5$ coloured red and $|\zeta| = 0.5$ coloured green) for UPO 4 in case $\boldsymbol{f}_\omega$. This UPO exhibits the growth and propagation of bending modes of the basic vortex tubes.

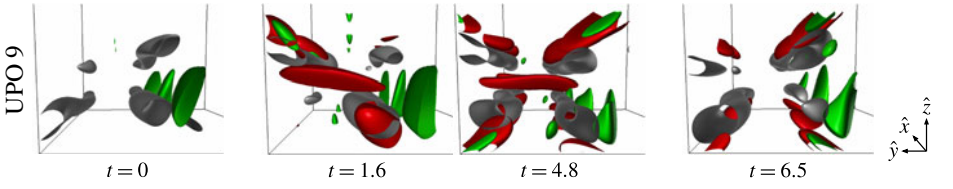


FIGURE 7. Isometric view of vorticity isosurfaces ($|\xi| = 4$ coloured grey, $|\eta| = 1.5$ coloured red and $|\zeta| = 1.0$ coloured green) for UPO 9 in case $\boldsymbol{f}_\omega$. It should be noticed that here we show a quarter of the domain to focus attention on the generation of transverse vorticity about the stagnation point.

(eight times) from the recurrent guesses. Here, as in the other low-amplitude UPOs, the three-dimensionality is provided by a dominant $k_z = 1$ long axial wavelength in the solutions. These first and second types of solution are clearly 'derivative' states, which can be smoothly traced back, via a small number of bifurcations, to the laminar solution as Re is reduced.

The third type of solution has larger $\hat{D}$ (excluding the outlying 2D state, UPO15), with UPOs 7 and 9 being prime examples. These UPOs exhibit some of the characteristics of the other solutions, i.e. shift-and-reflect and x-invariance symmetry breaking, but also more complex nonlinear behaviour too. This is generally manifested by larger-amplitude bending of axial vortex tubes and consequently more substantial production of transverse vorticity. The transverse vorticity is observed principally organised at the hyperbolic stagnation points, e.g. figure 7, but sometimes as localised toroidal vortex tubes about the basic axial vorticity, e.g. figure 8.

Figure 7 shows a quarter of the domain of UPO 9 and highlights the production of stagnation point transverse vorticity in the form of a thin vortex sheet. This occurs when the main axial vortex tubes are arranged such that adjacent vortices are bent towards each other, thereby increasing the local shear. In this region, the anti-parallel vortex lines will viscously reconnect if they approach closely enough, resulting in transverse vorticity which is then stretched into thin sheets by the background strain. This has some similarity to the transient growth enhancement in Taylor–Green vortices reported by Gau & Hattori (2014), where linear non-modal energy optimals show concentrated growth near the hyperbolic stagnation points. Following this production phase, the thin sheet decays due to viscosity and the axial vorticity is re-energised by the forcing. It should be noted that while this is observed in one vortex 'cell', other vortex tubes are meanwhile undergoing similar, but distinct, interactions out of phase with the one presented here. This makes quantitative analysis of precise isolated

https://doi.org/10.1017/jfm.2017.97 Published online by Cambridge University Press

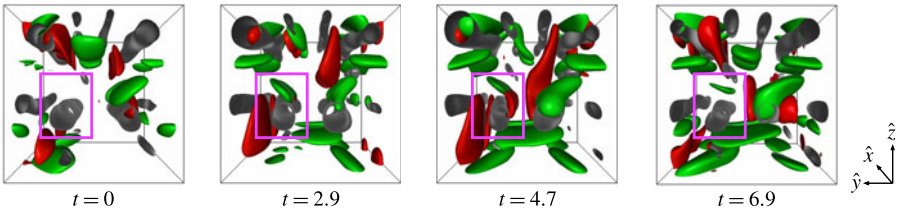


FIGURE 8. Isometric view of vorticity isosurfaces ($|\xi| = 4.5$ coloured grey, $|\eta| = 1$ coloured red and $|\zeta| = 1$ coloured green) for UPO 7 in case $\boldsymbol{f}_{\omega}$. Here, we show the full domain, including the subdomain of figure 9 (highlighted with a magenta box), in order to show the complexity of the processes occurring.

mechanisms a challenge, and indicates that precise periodicity of invariant solutions may be quite rare.

Figure 8 shows a close-up of an individual vortex tube in UPO 7 as it goes through another type of periodic cycle. The initially straight vortex tube gives rise to a growing patch of azimuthal vorticity (see $t = 2.9$ and $t = 4.7$) before it dies away (at $t = 6.9$). This evolution is reminiscent of the 'anti-lift-up' mechanism found in Antkowiak & Brancher (2007). Here, azimuthal streaks are found to be the (linear) transient energy growth optimal for vortex tubes, evolving into much larger-amplitude azimuthal vortices (rolls), as opposed to the generic lift-up mechanism in unidirectional shear flow of streamwise rolls growing into much larger streamwise streaks (Farrell 1988).

The existence of this 'new' transient growth mechanism could suggest the existence of an alternative type of self-sustaining process where the roles of the rolls and streaks (now defined relative to a different basic state so that, for example, 'streamwise-independent' means axisymmetric) are reversed. However, Rincon, Ogilvie & Cossu (2007) argued convincingly against this possibility in the context of the Keplerian disk problem, where the basic flow field is well known to be linearly stable. Here, our situation is rather different since the basic flow is unstable at this *Re* and so (as argued for the shear case above) the growing azimuthal rolls have more flexibility in manufacturing a (non-axisymmetric) wave mode which is neutral on average about the (now axially and radially varying) vortex to drive the (small) azimuthal streaks. The core problem that Rincon *et al.* (2007) identified, however, remains that the evolving finite-amplitude roll field interacts nonlinearly with itself and therefore is much more tightly constrained than the streak field in the SSP, which does not self-interact due to its streamwise independence.

Nevertheless, Goto *et al.* (2017) (see also Goto 2008, 2012) do report that 'daughter' vortices are often observed in vortically driven turbulence forming in the large-scale strain regions, perpendicular to their 'parents' in anti-parallel pairs, and conjecture that this may be a driving mechanism for the turbulent cascade process. Here, we see a similar picture emerge from the converged UPOs (e.g. figure 7), although we do not see the same scale separation and only one generation of offspring, both presumably due to the low Reynolds number used here.

The full dynamics of the UPOs is typically more complex than the individual interactions we have so far highlighted. For example, figure 9 shows the full domain of UPO 7, where the coherence between different cells appears to be lost. Furthermore, while we have discussed two possible transient growth mechanisms postulated before (Antkowiak & Brancher 2007; Gau & Hattori 2014), the 'base flow' in these UPOs is not really the low-*Re* laminar solution, but rather other averaged configurations arising from saturated instabilities such as the 2D states shown in figure 5.

https://doi.org/10.1017/jfm.2017.97 Published online by Cambridge University Press

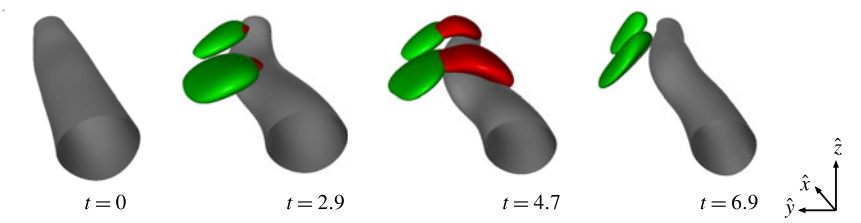


FIGURE 9. Isometric view of vorticity isosurfaces ($|\xi| = 4.5$ coloured grey, $|\eta| = 1$ coloured red and $|\zeta| = 1$ coloured green) for UPO 7 in case $\boldsymbol{f}_\omega$. It should be noticed that here we show a subdomain to focus attention on the generation of azimuthal vorticity around a vortex tube.

4. Discussion

Unstable solutions have been extracted directly from 3D body-forced turbulence for the first time at least at modest Re. Two distinct forms of forcing, unidirectional in either the velocity or the vorticity field, have been compared and the unstable orbits analysed to reveal possible sustaining mechanisms at work in these flows. When the forcing produces a unidirectional velocity with background shear, the UPOs found partition into two groups: those that originate from a linear instability of the base state – 'derivative' states – and those (generally of larger amplitude) that do not, which show the characteristic features of the SSP/VWI process (Hall & Smith 1991; Hamilton *et al.* 1995; Waleffe 1997). The key new realisation here is that SSP/VWI UPOs can be built upon a $u(y, z)\hat{\boldsymbol{x}}$ base flow when it is unstable. It has already been observed that SSP/VWI states can arise for a linearly stable base flow and subsequently co-exist with 'derivative' states connected to the base flow once it becomes linearly unstable at higher Re (e.g. channel flow). However, here the base flow becomes linearly unstable before (at lower Re) the SSP/VWI states arise. Our calculations indicate that 'derivative' UPOs and SSP/VWI UPOs are both dynamically important (embedded in the turbulent attractor) in the complex flows computed at least at $Re = 20$.

The situation is more complicated when the forcing is unidirectional in the vorticity. A number of steady and time-dependent two-dimensional states are extracted from the 3D turbulence, indicating that at this relatively low Re, 2D vortex dynamics can still play a role. Beyond these states, bending modes of the main vortex tubes provide the simplest three-dimensional behaviour. Transverse vorticity is then observed to arise from two different transient growth mechanisms: stagnation point generation (Gau & Hattori 2014) and local azimuthal generation (Antkowiak & Brancher 2007). The former is a feature of the global structure of the flow – driven vortices in periodic cells – and is difficult to avoid unless a single driven vortex is treated in isolation. The latter is particularly interesting in that it has recently been conjectured as the central process in the turbulent cascade (Goto *et al.* 2017) and may form a key stage in a new self-sustaining process. The existence of such a process would allow finite-amplitude states to exist without having to rely on a linear instability as an energy input. Put another way, in the absence of any such process, no other states should exist for any driven vortical state that is linearly stable for all Re. This would mean no turbulence, in contrast to the unidirectional shear situation where SSP/VWI exists. However, we have been unable to confirm this in the periodic flow configuration studied here, where multiple vortex tubes are driven in one domain

https://doi.org/10.1017/jfm.2017.97 Published online by Cambridge University Press

across which periodicity is assumed. This gives rise to a complicated array of linear instability modes which are either global (reaching across multiple vortex tubes) or localised to one tube (Gau & Hattori 2014).

One notable outcome of this work is the very limited success of recurrent flow analysis as Re is increased. Undoubtedly this is because the dimension of the chaotic attractor increases steeply, as indicated by the rapid destabilisation of UPOs continued up from lower Re. Future work will have to concentrate on this difficulty, which is clearly more pronounced in 3D than 2D (Lucas & Kerswell 2015), to make searches for recurrent flows as efficient as possible. The results presented here are the result of many months of wall time even with the substantial savings afforded by GPU-accelerated time stepping. Possible improvements may come from quotienting out the continuous symmetries (Willis, Cvitanović Avila 2013), which will reduce the overall degrees of freedom in the problem and remove the relative translations of states. A novel pre-processing of guesses prior to GMRES–Newton iterations to pre-condition or filter them with the goal of increasing the overall convergence rate may also improve efficiency (Farazmand 2016). Savings may also be made by employing a windowing method to concentrate numerical effort on some precise subdomain of interest, thereby focusing on localised behaviour and again reducing the overall degrees of freedom in the problem (Teramura & Toh 2014).

Acknowledgements

We would like to thank S. Goto for helpful discussions and for sharing his submitted manuscript (Goto *et al.* 2017) with us, and the anonymous referees for their helpful suggestions. We are also grateful for numerous free days of GPU time on 'Emerald' (the e-Infrastructure South GPU supercomputer: http://www.einfrastructuresouth.ac.uk/cfi/emerald) and the support of EPSRC through grant no. EP/H010017/1.

Supplementary material

Supplementary material is available at https://doi.org/10.1017/jfm.2017.97.

References

ANTKOWIAK, A. & BRANCHER, P. 2007 On vortex rings around vortices: an optimal mechanism. *J. Fluid Mech.* **578**, 295–304.

CHANDLER, G. J. & KERSWELL, R. R. 2013 Invariant recurrent solutions embedded in a turbulent two-dimensional Kolmogorov flow. *J. Fluid Mech.* **722**, 554–595.

CVITANOVIĆ, P. 1992 Periodic orbit theory in classical and quantum mechanics. *Chaos: An Interdiscip. J. Nonlinear Sci.* **2** (1), 1.

CVITANOVIĆ, P. & GIBSON, J. F. 2010 Geometry of the turbulence in wall-bounded shear flows: periodic orbits. *Phys. Scr.* **142**, 4007.

FARAZMAND, M. 2016 An adjoint-based approach for finding invariant solutions of Navier–Stokes equations. *J. Fluid Mech.* **795**, 278–312.

FARRELL, B. F. 1988 Optimal excitation of perturbations in viscous shear flow. *Phys. Fluids* **31**, 2093–2102.

GAU, T. & HATTORI, Y. 2014 Modal and non-modal stability of two-dimensional Taylor–Green vortices. *Fluid Dyn. Res* **46** (3), 031410.

GOTO, S. 2008 A physical mechanism of the energy cascade in homogeneous isotropic turbulence. *J. Fluid Mech.* **605**, 355–366.

GOTO, S. 2012 Coherent structures and energy cascade in homogeneous turbulence. *Progr. Theor. Phys. Suppl.* **195** (195), 139–156.

https://doi.org/10.1017/jfm.2017.97 Published online by Cambridge University Press

GOTO, S., SAITO, Y. & KAWAHARA, G. 2017 Hierarchy of anti-parallel vortex tubes in spatially periodic turbulence at high Reynolds numbers. *Phys. Rev. Fluids* (submitted).

HALL, P. & SHERWIN, S. 2010 Streamwise vortices in shear flows: harbingers of transition and the skeleton of coherent structures. *J. Fluid Mech.* **661**, 178–205.

HALL, P. & SMITH, F. T. 1991 On strongly nonlinear vortex/wave interactions in boundary-layer transition. *J. Fluid Mech.* **227**, 641–666.

HAMILTON, J. M., KIM, J. & WALEFFE, F. 1995 Regeneration mechanisms of near-wall turbulence structures. *J. Fluid Mech.* **287** (-1), 317–348.

HOPF, E. 1948 A mathematical example displaying features of turbulence. *Commun. Appl. Maths* **1**, 303–322.

KAWAHARA, G. & KIDA, S. 2001 Periodic motion embedded in plane Couette turbulence: regeneration cycle and burst. *J. Fluid Mech.* **449**, 291.

KAWAHARA, G., UHLMANN, M. & VAN VEEN, L. 2012 The significance of simple invariant solutions in turbulent flows. *Annu. Rev. Fluid Mech.* **44** (1), 203–225.

KREILOS, T. & ECKHARDT, B. 2012 Periodic orbits near onset of chaos in plane Couette flow. *Chaos: An Interdiscip. J. Nonlinear Sci.* **22** (4), 047505.

LAN, Y. H. & CVITANOVIĆ, P. 2004 Variational method for finding periodic orbits in a general flow. *Phys. Rev.* E **69** (1), 016217.

LUCAS, D. & KERSWELL, R. R. 2014 Spatiotemporal dynamics in two-dimensional Kolmogorov flow over large domains. *J. Fluid Mech.* **750**, 518–554.

LUCAS, D. & KERSWELL, R. R. 2015 Recurrent flow analysis in spatiotemporally chaotic 2-dimensional Kolmogorov flow. *Phys. Fluids* **27** (4), 045106.

MESHALKIN, L. & SINAI, Y. 1961 Investigation of the stability of a stationary solution of the system of equations for the plane movement of an incompressible viscous liquid. *Z. Angew. Math. Mech. J. Appl. Math. Mech.* **25**, 1700–1705.

RINCON, F., OGILVIE, G. I. & COSSU, C. 2007 On the self-sustaining processes in Rayleigh-stable rotating plane Couette flows and subcritical transition to turbulence in accretion disks. *Astron. Astrophys.* **463**, 817–832.

TERAMURA, T. & TOH, S. 2014 Damping filter method for obtaining spatially localized solutions. *Phys. Rev.* E **89** (5), 052910.

VAN VEEN, L. & GOTO, S. 2016 Subcritical transition to turbulence in three-dimensional Kolmogorov flow. *Fluid Dyn. Res.* **48** (6), 061425.

VAN VEEN, L., KIDA, S. & KAWAHARA, G. 2006 Periodic motion representing isotropic turbulence. *Fluid Dyn. Res.* **38** (1), 19–46.

VISWANATH, D. 2007 Recurrent motions within plane Couette turbulence. *J. Fluid Mech.* **580**, 339.

WALEFFE, F. 1997 On a self-sustaining process in shear flows. *Phys. Fluids* **9** (4), 883–900.

WILLIS, A. P., CVITANOVIĆ, P. & AVILA, M. 2013 Revealing the state space of turbulent pipe flow by symmetry reduction. *J. Fluid Mech.* **721**, 514–540.

WILLIS, A. P., SHORT, K. Y. & CVITANOVIC, P. 2016 Symmetry reduction in high dimensions, illustrated in a turbulent pipe. *Phys. Rev.* E **93** (2), 022204.

YASUDA, T., GOTO, S. & KAWAHARA, G. 2014 Quasi-cyclic evolution of turbulence driven by a steady force in a periodic cube. *Fluid Dyn. Res.* **46** (6), 061413.

https://doi.org/10.1017/jfm.2017.97 Published online by Cambridge University Press